Analysis of the spray field development on a vertical surface during water spray-quenching using a flat spray nozzle

W.J.J. Vorster, S.A. Schwindt, J. Schupp, A.M. Korsunsky

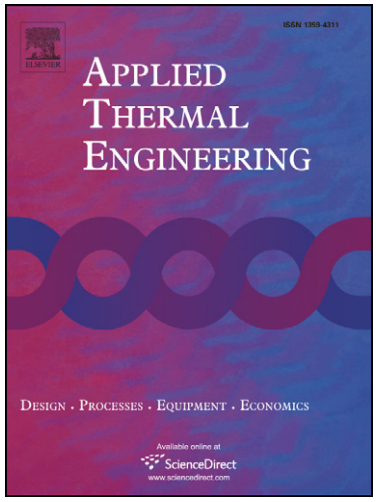

Analysis of the spray field development on a vertical surface during water spray-quenching using a flat spray nozzle

W.J.J. Vorster, S.A. Schwindt, J. Schupp, A.M. Korsunsky

PII: S1359-4311(08)00332-3
DOI: 10.1016/j.applthermaleng.2008.08.007
Reference: ATE 2595

To appear in: *Applied Thermal Engineering*

Received Date: 15 December 2007
Revised Date: 18 July 2008
Accepted Date: 9 August 2008

Please cite this article as: W.J.J. Vorster, S.A. Schwindt, J. Schupp, A.M. Korsunsky, Analysis of the spray field development on a vertical surface during water spray-quenching using a flat spray nozzle, *Applied Thermal Engineering* (2008), doi: 10.1016/j.applthermaleng.2008.08.007

Analysis of the spray field development on a vertical surface during water spray-quenching using a flat spray nozzle

W J J Vorster*, *willem.vorster@eng.ox.ac.uk*
S A Schwindt, *stefan.schwindt@eng.ox.ac.uk*
J Schupp, *jens.schupp@eng.ox.ac.uk*
A M Korsunsky, *alexander.korsunsky@eng.ox.ac.uk*

Department of Engineering Science, University of Oxford, Parks Road, OX1 3PJ, United Kingdom

Corresponding author: *willem.vorster@eng.ox.ac.uk*
tel: +44 1865 273812
fax:+44 1865 273906

Abstract - The aims of this study were (i) to conduct experimental spatially and time-resolved measurements of flow development on large heated surfaces during transient spray cooling operations, and (ii) to investigate and discuss the influence of spray cooling mechanisms such as bubble formation and the flow field development of the cooling fluid and how this affects heat transfer. Quartz plates were heated to above 500°C and then sprayed with pressurised water subcooled to 80K. High speed images of the quench process were collected at a rate of 3000 Hz making it possible to track the movement of the quench front as the plate cools below the Leidenfrost temperature of the fluid at that location. Observations showed that the relative importance of droplet-surface interactions decreases once the Leidenfrost temperature is reached on the plate: It was found that once the water contacts the surface, a water pool develops rapidly which grows larger as the pool floods the heated surface. Comparisons between the spatial flow development and heat transfer on the plate are made in order to describe these interactions more accurately. This information not only provides crucial input into process simulations, but is also useful to develop theoretical models of fluid-solid interaction describing the wetting of a heated component due to water spraying.

Keywords: Spray Quenching, Leidenfrost point, Critical heat flux, Flow development, Flat spray

1. INTRODUCTION

Thermomechanical processing is often used to alter the mechanical and microstructural properties of components with the aim of increasing strength and introducing favourable residual stress fields [1-5]. Spray quenching could be used to achieve this.

The purpose of this paper is to discuss the flow field development of a flat spray impinging on a vertical surface. The study involved two main sets of experiments that provided useful information about the wetting behaviour of a spray when cooling high temperature surfaces: in this paper high temperature refers to temperatures greater than the Leidenfrost temperature of the spray. It is the impression of the author that this research has not yet been done for spray cooling systems although similar studies have been performed for jet impingement cooling operations [6-9]. *For clarity of terms, it is mentioned that the parameters referred to as the minimum heat transfer coefficient and critical heat transfer coefficient in this paper take their usual meaning as would be the case in the framework of multiphase boiling heat transfer where the former is the magnitude of the coefficient at the Leidenfrost condition and the latter that measured at critical heat flux*

The first of the two sets of experiments involved spraying vertically oriented HS30 T6 aluminium alloy plates with pressurised water using a flat spray nozzle after heating the plates to approximately 500 °C. Infrared thermographs were collected of the plates during quenching. This experimental set-up is shown in Figure 1.

[Figure 1 here]

The spatio-temporal variations of heat flux and heat transfer coefficient were analysed by solving the three dimensional Fourier heat conduction equations. This was done with an inverse, backward-difference, optimisation scheme by applying the data from the thermographs as von Neumann boundary conditions to the optimisation model. The term “inverse” in this context refers to the calculation of heat flux boundary conditions by evaluating known sets of temperature gradients to solve the heat flux, as opposed to the forward

calculation that computes temperature. The term "optimisation" refers to computing the most likely spatial distribution of heat flux iteratively such that the requirements of thermal equilibrium of the system are satisfied. The optimisation scheme was specifically designed to compute the spatio-temporal distribution of heat flux from the experimentally measured thermographs. It was specifically design for this task because optimisation had to be done at each element in a grid of approximately 10000 elements corresponding to the pixels (unique data points) in the thermographs. The optimisation was done by iterating between possible solutions of the heat transfer coefficient that might result in the temperature change measured at that location. The complexity of the problem is somewhat convolved in that the solution is not unique. Each incremental change of heat transfer coefficient, $h_{i,j}$, at each location i,j in the grid affects the calculated spatial temperature distribution, therefore affecting the heat transfer coefficient calculation at all the other grid points. The optimisation scheme is illustrated in Figure 2.

[Figure 2 here]

The figure shows a series of six possible criteria that may occur at a node by assuming small changes in heat transfer coefficient results in a linear response of the temperature described by some function $\phi(h,T)$. In this figure the abscissa intersects the ordinate at the measured future temperature, $T_{\tau+\Delta\tau}$, at that location thus the optimised solution for this problem would be one where difference in predicted and measured points; $\min\{|T_1 - T_{\tau+\Delta\tau}|, |T_2 - T_{\tau+\Delta\tau}|\}$, reduces to a point on the abscissa. A temperature error range of 0.1 °C was specified as a convergence control for the process at each location. As in many other search algorithms, a new search direction is established by knowing the magnitudes of the calculated temperatures at that location with respect to the actual ones. For instance, considering that the calculated temperatures resulted in a situation as that illustrated in the top left schematic of Figure 2, then the two guessed boundary conditions results in calculated temperature T_1 that is less than T_2 which greater than the measured temperature, $T_{\tau+\Delta\tau}$. Now let's assume that $|T_1 - T_{\tau+\Delta\tau}| < |T_2 - T_{\tau+\Delta\tau}|$ then the new search direction in terms of the newly guessed heat transfer coefficient would be $h_{1new} = h_{1old}$ and $h_{2old} > h_{2new} > h_{\tau+\Delta\tau}$. It was decided that Fibonacci or golden section

search algorithms would in fact not result in increasing the solution time because of the dynamics of this specific problem, but this is not to say that more effective solutions to this optimisation scheme do not exist. This optimisation was done at each location on the grid, for each time increment (typically between 200 and 500 increments depending on the experimental conditions).

This strategy allowed computing the spatial and temporal variation in heat flux and heat transfer coefficient. In addition to this, parameters such as the spatial distribution of the point of minimum heat flux, Leidenfrost temperature, and first boiling crisis can be established. Studying these salient values of the boiling curve in space makes it possible to comment on the flow behaviour of the spray on the heated, vertically oriented, aluminium surfaces.

The spatial, and indeed the temperature dependence of the quench front is of particular interest in research focused on thermo-mechanical interactions during quench operations because of the large thermal gradients are produced upon wetting. The importance of understanding the development of thermal gradients resulting in thermal stresses is measured in that thermal stresses, in combination with temperature dependent thermal and mechanical properties, can introduce stresses exceeding the yield limit of the material, resulting in plastic flow and distortion, or cracking [10, 11]. Localised plasticity might induce significant residual stress and strain fields that can limit the useful life of quenched components or result in significant dimensional changes [12, 13].

Further experimentation was carried out aiming at visualising the movement of the quench front over a heated surface with the purpose of validating the numerically predicted behaviour of the quench front. In these experiments, a quartz sheet with the same dimensions as the aluminium alloy HS30 sheets was heated to 500°C and cooled as described previously. During these experiments the flow field development of the spray on the heated surface was studied by capturing images of the process at rates up to 3000 Hz. In addition to tracking the movement of the quench front, these experiments provided useful information about the bubbling behaviour on the surface, and other heat transfer mechanisms. The experimental set-up of these experiments

was exactly as that illustrated in Figure 1 except that the thermal imager was replaced with a high speed camera.

In all these experiments the heated surface can be considered large and the spray coarse. It is anticipated that this research will provide useful information concerning the flow field development of spray on heated surfaces.

2. EXPERIMENTAL PROCEDURES AND DATA ANALYSIS

In all of the above-mentioned experiments the JAQ1153, supplied by PNR UK Ltd, 60° flat spray nozzle was used. Figure 3 shows the spray characteristics of the nozzle. Figure 3a shows the total flow rate as a function of operating pressure as measured during experimentation. Figure 3b shows the velocity distribution along the long axis of the spray measured by *Phase Doppler Anemometry* (PDA) and Figure 3c the droplet size distribution along the long axis of the spray field measured using the same technique.

A patternator was used to study the spatial spray flux distribution at the same distance from the nozzle (200 mm) as for the aluminium alloy and quartz sheets during the quench experiments. The local spray flux results from the patternator were analysed and interpreted to compute the actual spray flux field by using a non-linear variational procedure and assuming a Gaussian spatial variation of spray flux field.

The Gaussian distribution of spray flux may be written as a function of two dimensional real space as in Eq. (1) in which A is the maximum value of spray flux located at position (X, Y) and, long and short axes along the Cartesian x and y coordinate directions with magnitude proportional to parameters B and C

$$\int_{-\xi}^{\xi}\int_{-\xi}^{\xi} Ae^{-0.5\left[\left(\frac{x-X}{B}\right)^2+\left(\frac{y-Y}{C}\right)^2\right]}dxdy. \qquad (1)$$

By considering the experimentally measured total flux constraints given in Figure 3a, the parameters in Eq. (1) are optimised to determine the flux field of the nozzle by choosing a minimising function in the form

$$q_i - f_i\left(x_i,\lambda_1,...,\lambda_n\right) = \sum_{j=1}^{n} \frac{\partial f_i}{\partial \lambda_j} \mathrm{d}\lambda_j \Bigg|_{x_i,\lambda} . \qquad (2)$$

In this equation q_i is the experimentally determined spray flux in m^3/m^2s measured at the location i of the patternator. The function $f_i\left(x_i,\lambda_1,...,\lambda_n\right)$ is the function value of a mathematical function chosen to describe the variation of the spray flux in space at location *i.* It is noted that the total flux, Q, should have the same magnitude as the integral of Eq. (1) integrated between the spray field limits ξ^+ and ξ^- which are determined by knowing the spray angle of the nozzle. This constraint allows formulating a description of the spray flux at location i in terms of the unknown amplitude value A as

$$f\left(x_i,\lambda_i\right) = \frac{Qe^{-0.5\left[\left(\frac{x-X}{B}\right)^2+\left(\frac{y-Y}{C}\right)^2\right]}}{\int_{-\xi}^{\xi}\int_{-\xi}^{\xi} e^{-0.5\left[\left(\frac{x-X}{B}\right)^2+\left(\frac{y-Y}{C}\right)^2\right]} dxdy} .$$

Integrating the exponential function above results in

$$f\left(x_i,\lambda_1...\lambda_n\right) = \frac{Q\cdot e^{-0.5\left[\left(\frac{x-X}{B}\right)^2+\left(\frac{y-Y}{C}\right)^2\right]}}{\frac{-\pi}{2}C\cdot B\left[\mathrm{erf}\left[\frac{1}{\sqrt{2}}\left(\frac{X-\xi}{B}\right)\right]-\mathrm{erf}\left(\frac{1}{\sqrt{2}}\left(\frac{X+\xi}{B}\right)\right)\right]\left[\mathrm{erf}\left[\frac{1}{\sqrt{2}}\left(\frac{Y-\xi}{C}\right)\right]-\mathrm{erf}\left(\frac{1}{\sqrt{2}}\left(\frac{Y+\xi}{C}\right)\right)\right]} \qquad (3)$$

The right hand side of Eq. (2) is the set of gradient functions of Eq. (3) with respect to the fitting constants B, C and position of maximum function value X and Y.

A 'best fit' solution $f\left(x_i,\lambda_1...\lambda_n\right)$ to the experimentally measured spray flux is found by iteration. The parameter $\mathrm{d}\lambda_j$ in Eq. (2) is a measure of the change in fitting parameters after iteration *n*. The iteration procedure is continued until the scalar valued function $\mathrm{d}\lambda$ converges to a predetermined value usually set to the order of 1e-6.

[Figure 3 here]

The result of the analysis of the spray flux field of the nozzle used operating under 5 bar pressure is illustrated in Figure 4a, clearly showing good agreement between measurement and prediction. In this figure the surface indicates the predicted value of spray flux in Cartesian coordinates system where the *z*-axis is a measure of the magnitude of the spray flux at that location. The spray flux distribution of the long and short axis of this nozzle is shown as a function of operating pressure in Figure 4b.

As will become clear later, the experimental data seems to suggest a very strong correlation between heat transfer and spray flux.

[Figure 4 here]

2.1. Determination of Spatio-Temporal Spray Heat Flux

These experiments consisted of heating 100-mm by 100-mm by 3-mm thick aluminium alloy HS30 T6 plates well into the film boiling regime of water at 1 atm and then spray cooling them with 80K subcooled water using a 60° flat spray nozzle (JAQ1153). During spraying an Agema 900 thermal imager was placed at the opposite side of the plate, which was painted with a high temperature black matt paint, to record the transient temperature distribution of the surface of the plate during the quench. The Agema system is cryogenically cooled and has a working temperature range of -30 to +1500 °C with a sensitivity of 0.08 °C at +30 °C. Out of the three possible temperature measurement ranges, the second was chosen which allowed accurate

temperature measurement in the range between 100°C and 600°C. The thermographs were exported as video sequences or single frames of temperature distribution at each time instant during the recording. The Forward Looking Infrared (FLIR) Systems Inc. analysis software enabled the user to view and export the temperatures recorded in a matrix of 136 by 272 temperature data points. This pixel number determines the field of view and the spatial resolution obtained using the 20° lens.

Calibration of the camera was done by heating similar plates to above 500 °C however, during these experiments, a number of K-type thermocouples were embedded into the plates from which the transient temperature behaviour of the plates were recorded simultaneously. Exact time discrimination of the thermal images and thermocouple measurements were ensured by using a light diode trigger which triggered data logging of both devices simultaneously as spraying initiated. As part of the calibration procedure the emissivity of the black matt paint was calculated by doing an energy balance of the radiation flux exchange between the environment, thermal imager and heated aluminium plates.

Initiation of critical heat flux (CHF) regime at the geometrical centre of the spray during the transient quench experiments was ensured by containing the spray to an 80-mm by 80-mm area on the plate. This was done to avoid edge effects due to droplet stagnation inevitably resulting in the initiation of the critical heat flux at these locations, consequentially producing unreliable heat transfer distribution data.

Thermographic data handling. Following the quenching of the aluminium sheets, full-view thermographs were cropped to plate edge. A surface plot of a typical spatial temperature data set (thermograph) is shown in Figure 5a. It is clear that the data contains a degree of spatially distributed noise. Figure 5b shows a plot of the temperature in the time domain also showing considerable noise. 'Time dependant noise' might cause convergence problems of the inverse heat flux calculation, especially during steep temperature gradients experienced during e.g. the CHF regime.

Careful consideration of the nature of the problem suggests that temporal data smoothing is a reasonable approximation if it is assumed that the temperature history of the aluminium during this process can be represented by a smooth, continuous and differentiable function of time. This assumption seems physically justified, and well-supported by literature. On the other hand, spatial smoothing might exacerbate errors during analysis, since it is impossible for the analyst to guess the spatial temperature behaviour on a solid surface during the spray quenching process due to highly non-linear heat transfer interactions between the environment and the solid, including instantaneous convection, radiation, transient conduction within the material, phase change of the quenchant, and possible heat generation due to plasticity and (microstructural) phase transformation.

Noise reduction was therefore only done temporally by fitting a smoothing function to the temperature data points (τ_i, T_i), $i = 1,...,n$ at each location j (here the 2D temperature matrix with n rows and m columns is reduced to a temperature vector with $n \times m$ entries) in the image using a least squares formulation with the objective function

$$P = \sum_{i=1}^{n} \left(T_i(\tau_j) - \sum_{l=1}^{n} a_l \Gamma_{i,k}(\tau_j, \gamma, \zeta) \right)^2 \qquad (4)$$

where $a_l \Gamma_{i,k}(\tau_j, \gamma, \zeta)$ is the B-type spline with coefficients a_l of order k (k = 4 typically for B-splines) with knots $\zeta_1,\ldots,\zeta_n$ denoted by ζ, which do not have to coincide with data points, and smoothing parameter γ [14-16]. In this equation P is a measure of the sum of the errors between the measured temperature data set in the time domain at location i and the best fit B type spline representation of the time dependant temperature at that location. It's worth mentioning that this formulation was chosen for this particular application though it could very easily be extended to take care of variable knots or smoothing parameters.

To find the solution to the objective function P which minimises the error between the predicted and measured values of temperature at each location the gradient of P is evaluated with respect to the fitting parameters a_l and Γ_i as

$$\nabla P_{a_l,\Gamma_i} = 0 \qquad (5)$$

from which the least squares spline fit is obtained.

A typical fit produced by choosing the objective function Eq. (4) and seeking the solution of the system in Eq. (5) is illustrated in Figure 5b, showing satisfactory correlation between the fit and the original data.

The transient quench experiments were analysed by applying the temporally smoothed temperature data as von Neumann boundary conditions to an inverse heat flux calculation. The output to the analysis is the heat transfer coefficient at each spatial discretization which can be plotted as a data point in space together with that of the rest of the domain to produce a 2D representation of the heat transfer coefficient and heat flux experienced on the surface [17].

[Figure 5 here]

Figure 6a to Figure 6d illustrate the computed time-resolved development of the heat transfer coefficient on the surface of an aluminium specimen cooled with a water spray operating under 5 bar pressure and the same fluid conditions as specified previously. Figure 6a illustrates the film boiling heat transfer coefficient. This heat transfer coefficient distribution is seen to be reasonably constant over the entire surface of the specimen and considerably smaller in magnitude as compared to that reached in Figure 6b to Figure 6d. Figure 6b illustrates the situation when critical heat flux is initiated on the surface of the plate. The location of the maximum shown in this figure corresponds to the geometrical centre of the nozzle where the greatest spray flux exists. The movement of the CHF towards the edge of the specimen is visible in Figure 6c and Figure 6d.

The movement of the CHF occurs as the temperature in the centre of the specimen cools below T_{CHF} and then further below the boiling incipience temperature.

[Figure 6 here]

2.2. High Speed Imaging of Spray Field

A quartz (fused SiO_2) plate was manufactured to the same dimensions as the aluminium specimen. The plate was heated to about 500 °C and then sprayed with water under the same conditions as that used in the previous experiments. A high speed camera was placed at the opposite side of the plate with respect to the nozzle and recorded the flow field development on the surface of the quartz as it cooled to room temperature during the spray quenching.

The Phantom 7.2 high-speed camera was used for image collection. The camera allowed manipulation of image resolution and data collection frequency. Due to the very short exposure time of the imaging chips, Dedocol spot lights were used (approximate strength of 731000 lx) and strategically placed to reduce any potential temperature interference through radiation with the quartz specimen.

The aperture of the camera was closed to provide a large depth of field to enable capturing the behaviour of the flow field on and away from the surface. A frame rate of 3000 fps was chosen for the experiments analysed in this paper. As in the aluminium alloy quench experiment, the spray was contained to an 80 mm by 80 mm inner section of the total quartz surface area to suppress edge effects.

Observations made during high speed data capturing. A number of observations made significant to the numerical analyses of the temporal heat transfer coefficient development can be pointed out here. The first is the verification the film boiling regime during which droplets makes partial contact with the heated surface. In this boiling regime, droplets as seen to bounce off the surface, as wetting is not established. Following this is

the initiation of surface wetting at the centre of the specimen (corresponding to the centre of the nozzle) and the movement of the quench front (and hence CHF front) towards the edges of the specimen. This is in accordance to previous speculation made by the authors of Ref. [18] in which exactly this type of CHF development was discussed. Initial fluid solid contact is observed to cause complete evaporation of droplets in the location of the geometrical centre of the spray producing considerable amounts of steam.

Once the centre of the quartz plate is cooled sufficiently, the quench front moves radially outwards towards the edges of the plate in the form of unstructured, 'concentric' sections, until the outer edges of the spray containment or spray flux field are reached. When this happens the movement of the quench front is slowed down until enough water collects in the pool on the surface, which then forces the water further towards the edge of the plate.

During the expansion of the quench front intense vorticial motion is induced in the wetted region of the plate by the combined interaction of droplets, now contacting the surface which is below the Leidenfrost temperature, and fluid and bubble flow as the pool of water is forced radially outward. It is observed that main mechanism of heat transfer due to bubbling in the wetted area is due to secondary bubbles formed upon droplet impact. Primary bubbling, i.e. as would be observed at boiling incipience under pool boiling conditions was not found to be prominent at all. It is speculated that the intense vorticial motion in the pool reduces bubble growth times, as bigger secondary bubbles move over the quartz surface and coalesce with primary ones. It was found that, if not punctured on route, secondary bubbles ended up at the quench front. This could result in local dry out which could have an effect on the oscillatory motion of the quench front, often observed during transition boiling studies [19, 20].

It can therefore be concluded that, while the size of the pool is smaller than the spray field, heat is transferred away from the heated surface by (i) the mixing of newly impinged, cold fluid with the heated pool, (ii) thin film evaporation due to droplet impingement and formation of secondary bubbles, (iii) the transport of heat across the pool of water by secondary bubbles and fluid turbulence, and (iv) coalescence of secondary bubble

with the fewer primary bubbles found at the edge of the quench front. Similar results were obtained and is discussed elsewhere [21-23].

Once the area of the pool on the surface of the quartz exceeds the area of the spray field, the motion of the quench front decelerates, until enough water accumulates that then forces the pool further outwards as the momentum of the pool increases proportionally to its volume. It is speculated that once this happens the quench front should behave very similarly to that experienced during jet impingement. With the quench front behaviour during jet impingement cooling being analogous to flow boiling situations, it can be expected to see an increase in the quench temperature. Figure 7a to Figure 7d shows a series of images taken of the development of the wetted region showing droplets bouncing off the surface due to impartial wetting, secondary bubbling, stagnation of secondary bubble at the quench front and the accumulation of water as the wetted region becomes larger than the spray field.

[Figure 7 here]

3. RESULTS

The results presented here concern the interpretation of the spatio-temporal distributions of the heat transfer coefficient with the purpose of determining the spatial distribution of the Leidenfrost temperature and the temperature at the initiation of the critical heat flux, T_{CHF}. Such results are of particular interest because, in the first instance, these temperatures could be used to reconstruct the development of the quench front over the surface of the specimen, allowing direct comparison to the fields observed with the high-speed camera. Similarly, the movement of the CHF front can be studied. To the best knowledge of the authors, full field (2D) studies of the decay of the CHF have not been reported for water sprays yet. One-dimensional measurements of the decay of the CHF wave due to jet impingement have previously been reported using thermocouples [6, 7, 9].

To determine each salient value, e.g. T_{CHF} or T_{MIN}, Gaussian distributions were fitted to the boiling curve at the position of interest. This fitting approach is widely used in scientific practice, e.g. when residual elastic strains are computed by 'single peak fitting' of X-ray or neutron diffraction patterns [24]. In the present analysis, the function values of the boiling curve in the temperature domain of interest were subjected to a rotation in the *h, T* plane, after which a single Gaussian peak was fitted and the desired salient value was determined. Once the salient temperatures were established, heat fluxes corresponding to these temperatures were computed.

3.1. Spatial Distribution of the Critical and Minimum Heat Flux

Figure 8a is a surface plot of the magnitude of the heat transfer coefficient achieved during CHF. It is evident from the figure that a maximum value of CHF in the spray field is reached at the geometrical centre of the spray which decays towards the edges of the specimen. Before reaching the edge of the specimen, the magnitude of CHF is seen to increase. It is speculated here that this is a result of water accumulation on the edges of these specimens and will not necessarily be present when larger heater surfaces are used or when spraying occurs well within the heated domain.

[Figure 8 here]

Figure 8b is a contour plot of T_{CHF} indicating that the temperature at which CHF is reached within the spray field is not very dependent of the spray flux distribution. Figure 9a shows a contour plot of the spatial distribution of the minimum heat transfer coefficient. Comparatively little variation in the magnitude of the minimum heat transfer coefficient is evident. A contour plot of the Leidenfrost temperature reached on the specimen surface shown in Figure 9b indicates that the Leidenfrost temperature does vary more than the T_{CHF} and may be proportional to the spray flux distribution.

[Figure 9 here]

3.2. The Movement of the CHF Wave and the Quench Front

Figure 10a illustrates the quench front calculated for different time steps during the experiment in which each ring in the figure corresponds to a different time step. The quench front is seen to move radially outwards. Indications of quench front oscillations are visible in the figure. Figure 10b shows a similar plot of the position of the CHF wave as it moves across the surface. The movement of CHF is clearly more structured than that of the quench front, as it sweeps across the surface in the form of concentric ellipses. In previous studies [9], the movement of the CHF and quench front was further analysed to determine the so-called CHF and quench front velocity. In these studies differences in velocity were calculated for different materials. It was concluded that the velocities differ depending on the material. This is to be expected due to the difference in the thermal properties of the materials. Such results should in fact be presented in dimensionless form to include thermal scaling. Quench and CHF velocities are therefore not computed or presented in this paper.

The black rings in Figure 10b correspond to when the wetted region is still within the spray field and the blue corresponds to when the pool has moved outside of this field. In the former case a well structured development of the CHF is clearly noticeable.

[Figure 10 here]

4. DISCUSSION

Before comparing the results discussed so far, it is worth pointing out the following concerning the above analysis of the boiling curve resulting from a spray quenching. During the development of this work, greatest

care was taken to reduce errors in the analysis in as far as possible. This was done specifically to decrease analytical uncertainties and was achieved by limiting convergence criteria of all numerical studies and optimisation schemes as specifically set out in the above discussions.

In these, and spray quench experiments done using different nozzle types it was found that the quench temperature never varied significantly from the Leidenfrost temperature. In quench experiments/processes this is significant because efficient heat exchange only occurs at temperatures below wall saturation temperature differences less than approximately 170 K. The significance of this becomes clearer when considering operations where high instantaneous heat flux removal is necessary for safety purposes e.g. nuclear core cooling or fire extinguishing. It is also expected that the temperature at minimum heat flux of a spray would not be greatly influenced by sub-cooling as would be the case in bath quench operations where a difference in subcooling of 80 K could result in the initiation of surface wetting to span over up to 700 C which makes the analysis of bath quench operation so complex.

It should also be pointed out that is has been proposed that the magnitude of the CHF experienced during a spray operation is desirable for high heat flux removal operation such as in cooling of electronics though the very narrow heat flux domain between boiling incipience and minimum heat flux suggest that small shifts in component surface temperature would result in a dramatic decrease of heat flux in the cooling and in the heating direction. This could result either in over heating or significant cooling of the component which may lead to residual stress formation that could result in failure of brittle components such electronic chips.

It should finally be pointed out that the quench temperature experienced during jet impingement [25] is between that experienced by a water spray and a bath quench. It is therefore indeed possible to design a quench operations in such a manner that would result in favoured residual stress distributions (such as in the case of shot peeing for instance) and microstructural characteristics in the component with reduced distortion or dimensional changes. Figure 11 is included for comparison of the differences in the boiling heat flux behaviour of a spray and that experienced during a bath quench for water with 80 K subcooling. The boiling

curve of the bath quench in the figure was constructed by evaluating the salient values using standard solutions found in the literature [26-30].

In addition to the above general conclusions the following specific conclusions relating to this research can be drawn: Comparing the spray flux distribution (Figure 4a) derived from the patternator results with the decay of the CHF on the aluminium specimen surface (Figure8a) suggests a strong correlation between these parameters. Inside the spray containment a monotonic decrease in the CHF is observed similar to that of the spray flux. The increase in the CHF outside the containment and the spray field suggests a change of heat transfer mechanism from that resulting from droplet interaction with the heated surface to one influenced by the fluid being forced (by momentum) causing flooding and stagnation of fluid at the specimen edges; hence the increase in the CHF towards the edge of the specimen. In contrast to the CHF and Leidenfrost temperature, the T_{CHF} and minimum heat flux does not seem to be too affected by the spray field though some degree of proportionality does exist.

As expected the quench front is unstructured as shown in Figure 7 and Figure 10a being resulting from quench front oscillations as the material periodically cools and heats as heat is conducted in and out of the material at the front. Dry out of the quench front may result from secondary bubble being transported to the front due to the outward motion of the wetted region. Secondary bubbles were often noticed to become stagnant at the front until it is either punctured by impinging droplets or due to bubble growth.

[Figure 11 here]

The extreme heat removal during CHF causes a well structured propagation wave of the CHF moving radially towards the edges of the specimen in a series of concentric ellipses. The time dependent location of the CHF can further be interpreted to calculate CHF wave velocities but is not included in this discussion.

Understanding the spatial distribution and motion of the various salient values of the boiling curve during quench operations forms the basis of quench process modelling. Residual stress formation and warping is directly proportional to the rate of heat removal rate and the mechanism used to achieve this.

5. CONCLUSIONS

It can be concluded here that the spatial distribution of the CHF is directly proportional to the spray flux field, both decreasing monotonically away from the geometric centre of the spray. Little correlation between the spray flux, T_{CHF} and minimum heat flux is evident. The movement of the quench front can be suitably calculated using a 3D inverse calculation by applying spatial temperature data, such as that contained in a thermograph, as Neumann boundary conditions. Similarities in quench front behaviour are noticed between the numerically predicted and high speed observation of the quench front particularly concerning the oscillatory motion of the front.

High speed imaging of the quench process suggest that the main heat transfer mechanisms in the wetted region are due to secondary bubbling and intense vortical fluid motion. Primary bubbling in what should be 'nucleate' boiling regime was not evident though this does not rule out the possibility of nucleate boiling being prominent under different surface conditions e.g. surface roughness and surface contamination. During these experiments it was observed that primary bubble growth was inhibited by the intense vortical fluid motion and coalescence of primary bubble with secondary ones transported from the inner regions of the wetted domain to the quench front. It is anticipated that heat is also removed by thin film evaporation as droplets impacts with the wetted region to form secondary bubbles or during secondary bubble puncturing at the quench front.

Understanding the heat transport phenomena occurring during quench operation will result in more realistic process analyses which have the advantage of enabling the accurate prediction of microstructural, dimensional and residual stress field characteristics of the quenched component.

6. REFERENCES

[1] Newman, M.L., Robinson, B.J., Sehitoglu, H., Dantzig, J.A., Deformation, residual stress, and constitutive relations for quenched w319 aluminum, Metallurgical and Materials Transactions A: Physical Metallurgy and Materials Science, 34 A (7) (2003) 1483-1491.

[2] Schroder, R., Influences on development of thermal and residual-stresses in quenched steel cylinders of different dimensions, Materials Science and Technology, 1 (10) (1985) 754-764.

[3] Sjostrom, S., Interactions and constitutive models for calculating quench stresses in steel, Materials Science and Technology, 1 (10) (1985) 823-829.

[4] Koc, M., Culp, J., Altan, T., Prediction of residual stresses in quenched aluminum blocks and their reduction through cold working processes, Journal of Materials Processing Technology, 174 (1-3) (2006) 342-354.

[5] Burnett, J.A., Prediction of stress history in carburized and quenched steel cylinders, Materials Science and Technology, 1 (10) (1985) 863-871.

[6] Mozumder, A.K., Woodfield, P.L., Ashraful Islam, M., Monde, M., Maximum heat flux propagation velocity during quenching by water jet impingement, International Journal of Heat and Mass Transfer, 50 (7-8) (2007) 1559-1568.

[7] Mitsutake, Y., Monde, M., Heat transfer during transient cooling of high temperature surface with an impinging jet, Multiphase Science and Technology, 12 (3-4) (2000) 177-194.

[8] Hammad, J., Mitsutake, Y., Monde, M., Movement of maximum heat flux and wetting front during quenching of hot cylindrical block, International Journal of Thermal Sciences, 43 (8 SPEC ISS) (2004) 743-752.

[9] Woodfield, P.L., Monde, M., Mozumder, A.K., Observations of high temperature impinging-jet boiling phenomena, International Journal of Heat and Mass Transfer, 48 (10) (2005) 2032-2041.

[10] Vorster, W.J.J., Van Der Watt, M., Venter, A.M., Oliver, E.C., Prakash, D.G., Korsunsky, A., Quench modelling and investigation into the influences of boiling phase incipient temperatures shifts due to quenchant hydrodynamics on residual stress formation, Heat Transfer Engineering, In Press (2008).

[11] Vorster WJJ, van der Watt M, Venter A, Oliver EC, Prakash DG, Korsunsky AM. Residual elastic strain measurements and modelling of AISI 316L stainless steel cylinders subjected to spray quenching. In: 5th International Conference on Heat Transfer, Fluid Mechanics and Thermodynamics, South Africa (2007).

[12] Topic, M., Bucher, R., Vorster, W., Zhang, S.Y., Mcgarth, P., Korsunsky, A.M., Residual stress in laser bent steel components, Material Science Forums, 524 (2006) 299-304.

[13] Topic, M., Mcgrath, P., Vorster, W.J., Zhang, S.Y., Bucher, R., Venter, A., Korsunsky, A.M., Multi-scan laser forming: Synchrotron strain scanning and microstructure evolution, Journal of Strain Analysis, n Press, Corrected Proof (2006).

[14] Inoue, H., Least-squares smooth fitting for irregularly spaced data: Finite-element approach using the cubic b-spline basis., Geophysics, 51 (11) (1986) 2051-2066.

[15] Yoshimoto, F., Harada, T., Yoshimoto, Y., Data fitting with a spline using a real-coded genetic algorithm, CAD Computer Aided Design, 35 (8 SPEC) (2003) 751-760.

[16] Wang, G., Wang, Z., Shou, H., Smooth fitting of b-spline surfaces with strict interpolation conditions, Ruan Jian Xue Bao/Journal of Software, 9 (9) (1998) 696-698.

[17] Vorster WJJ, Korsunsky AM. Visualisation of the Temperature Field and Spatio-Temporal Heat Transfer Coefficient on a Flat Vertical Surface During a Water Spray-Quenching. In: 13th International Heat Transfer Conference, Sydney, Australia, (2006).

[18] Hall, D.D., Mudawar, I., Predicting the impact of quenching on mechanical-properties of complex-shaped aluminum-alloy parts, Journal of Heat Transfer-Transactions of the Asme, 117 (2) (1995) 479-488.

[19] Witte, L.C., Lienhard, J.H., On the existence of two "transition" boiling curves., International Journal of Heat and Mass Transfer, 25 (6) (1982) 771-779.

[20] Wang, S.W., Weisman, J., Post-critical heat flux heat transfer: A survey of current correlations and their applicability., Progress in Nuclear Energy, 12 (2) (1983) 149-168.

[21] Chen, R.-H., Tan, D.S., Lin, K.-C., Chow, L.C., Griffin, A.R., Rini, D.P.: Droplet and bubble dynamics in saturated fc-72 spray cooling, American Society of Mechanical Engineers, New York, NY 10016-5990, United States, Conference, Location, 2005.
[22] Rini, D.P., Chen, R.-H., Chow, L.C., Bubble behavior and heat transfer mechanism in fc-72 pool boiling, Experimental Heat Transfer, 14 (1) (2001) 27-44.
[23] Rini, D.P., Chen, R.-H., Chow, L.C., Bubble behavior and nucleate boiling heat transfer in saturated fc-72 spray cooling, Journal of Heat Transfer, 124 (1) (2002) 63-72.
[24] Vorster, W.J.J., Zhang, S.Y., Golshan, M., Laundy, D., Dini, D., Korsunsky, A.M., Comparison of x-ray diffraction measurement of residual elastic strains: Monochromatic beam and image plate versus white beam energy-dispersive analysis, The Journal of Strain Analysis for Engineering Design, 42 (2007) 23-37.
[25] Liu, Z.-H., Wang, J., Study of film boiling heat transfer for water jet impinging on high temperature flat plate, International Journal of Heat and Mass Transfer, 44 (13) (2001) 2475-2481.
[26] Bergles, A.E., Thompson, W.G., Relationship of quench data to steady-state pool boiling data, International Journal of Heat and Mass Transfer, 13 (1) (1970) 55-68.
[27] Dhir, V.K., Purohit, G.P., Subcooled film-boiling heat transfer from spheres., Nuclear Engineering and Design, 47 (1) (1978) 49-66.
[28] Frederking, T.H.K., Clark, J.A.: Natural convection film boiling on sphere, Conference, Location, 1962.
[29] Carbajo, J.J., Study on the rewetting temperature., Nuclear Engineering and Design, 84 (1) (1985) 21-52.
[30] Chambre, P., Elias, E., Boiling heat-transfer during rewetting, Nuclear Engineering and Design, 50 (3) (1978) 353-363.

7. FIGURES

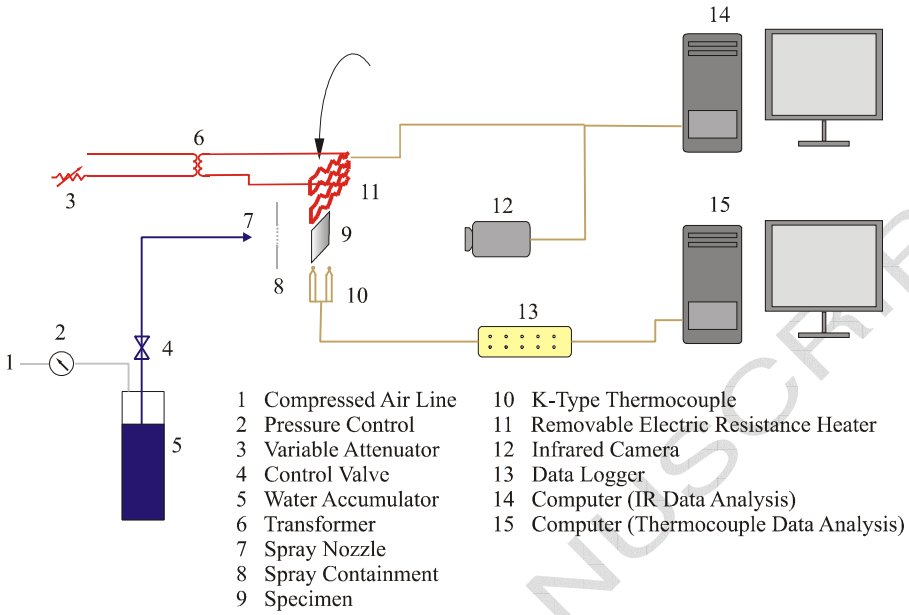

Figure .1. Schematic of the experimental set up used in the heat transfer characterisation experiments.

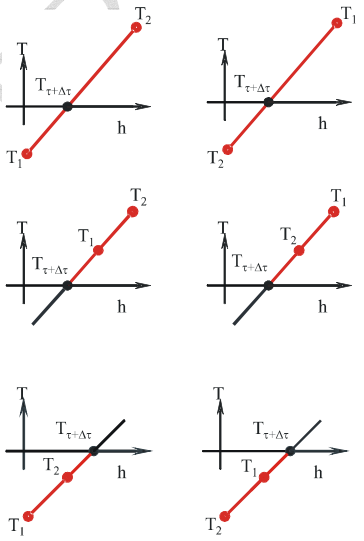

Figure .2. Schematic showing the possible situations used to determine the search direction in the inverse heat transfer coefficient calculation.

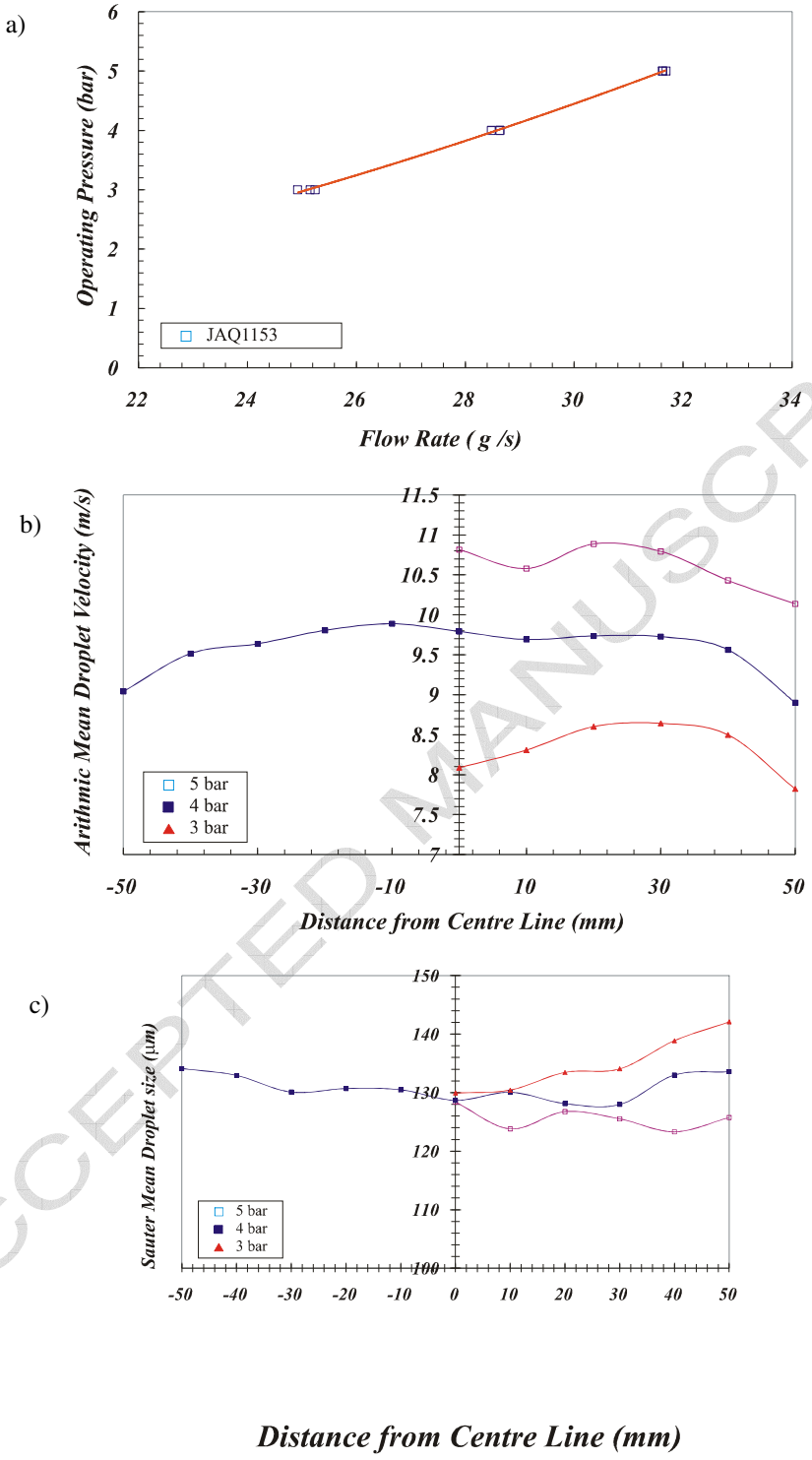

Figure .3. Plot of a) the total flow rate as a function of operating pressure, b) droplet velocity and c) droplet size distribution along the long axis of the spray.

a)

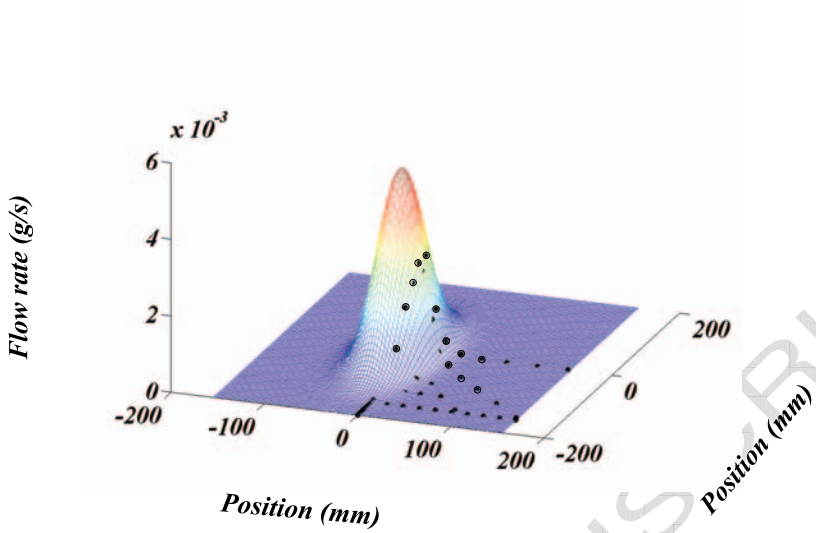

b)

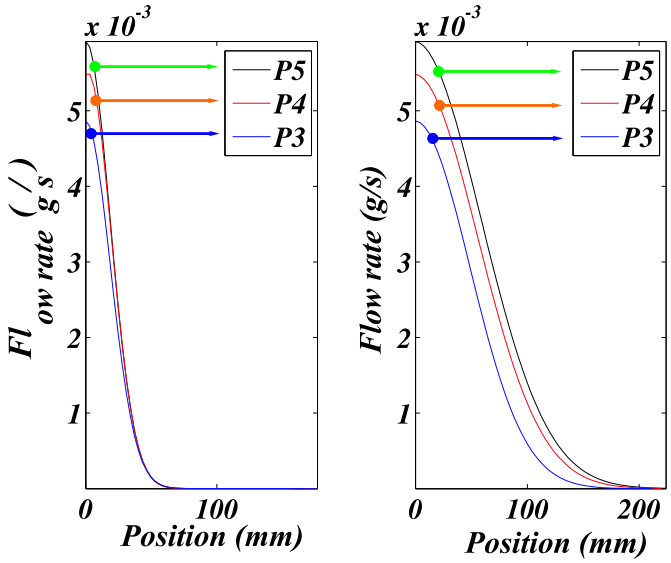

Figure .4. a) 2D Spray flux distribution of JAQ1153 and b) spray flux along the nozzles long and short axis.

a)

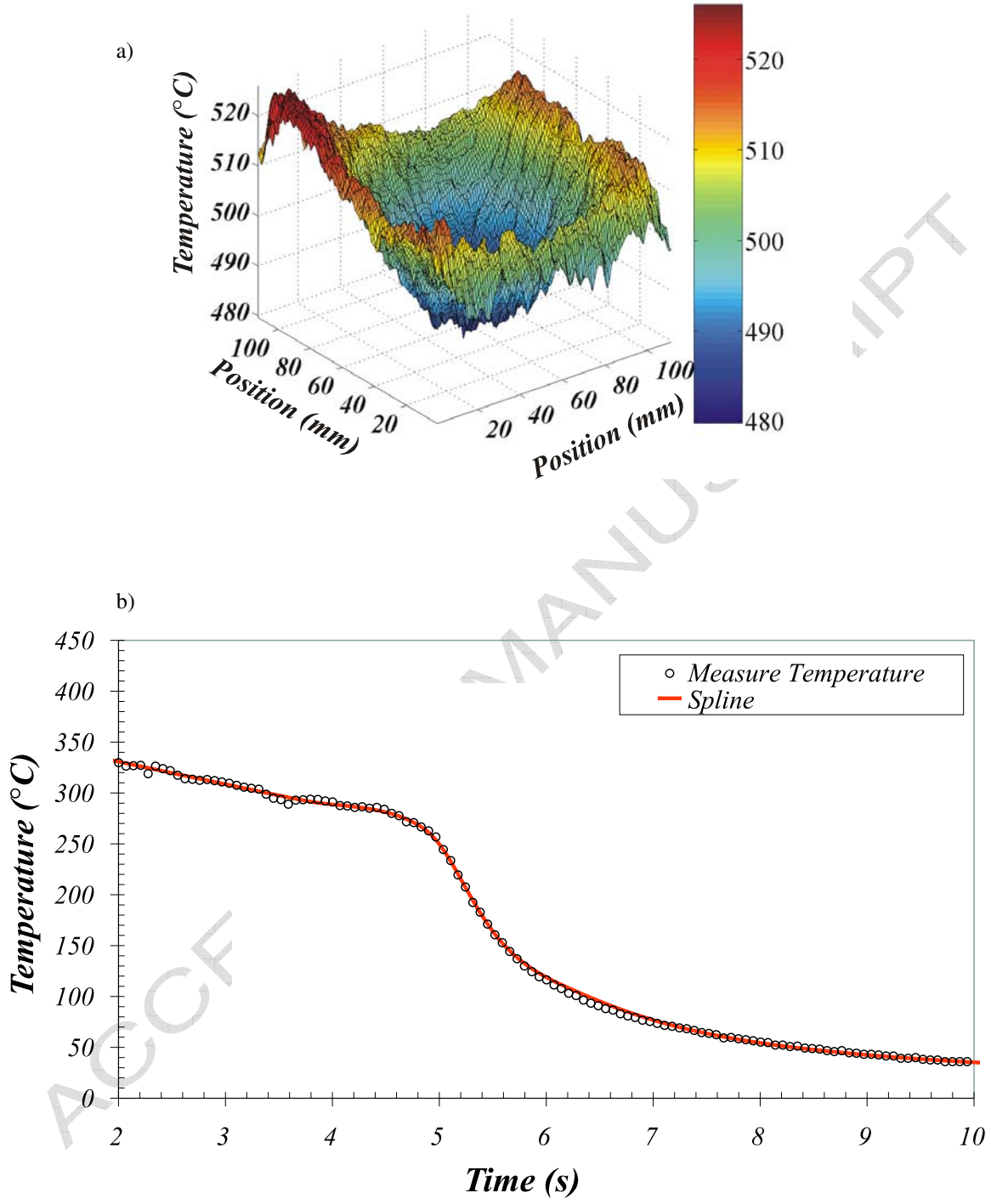

Figure .5. a) Surface plot of a typical thermograph measured using Infrared thermography. b) Temporally fitted temperature response of a point on thermograph.

a)

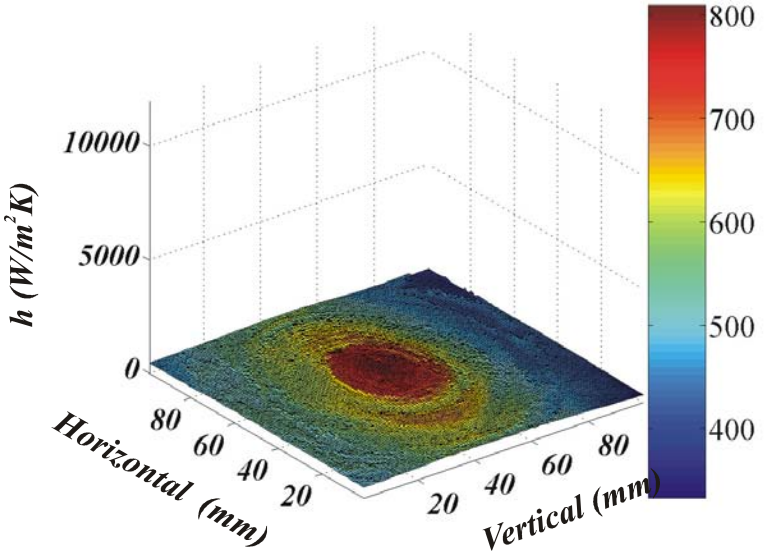

b)

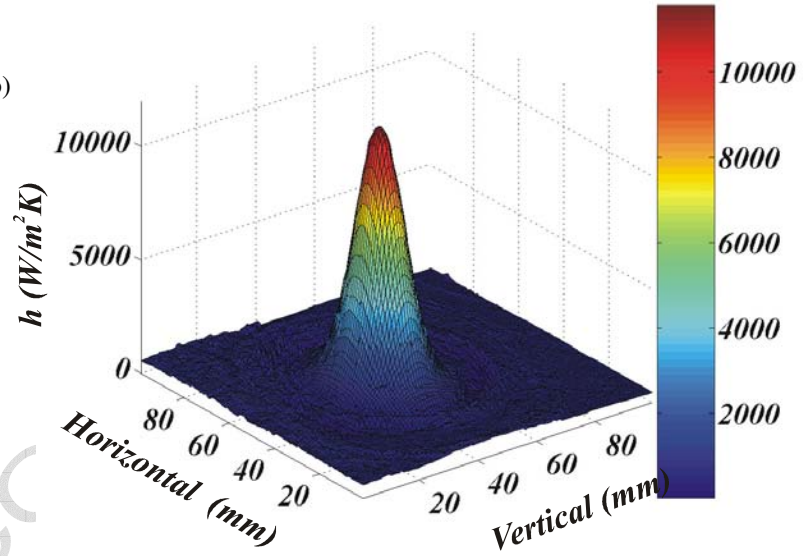

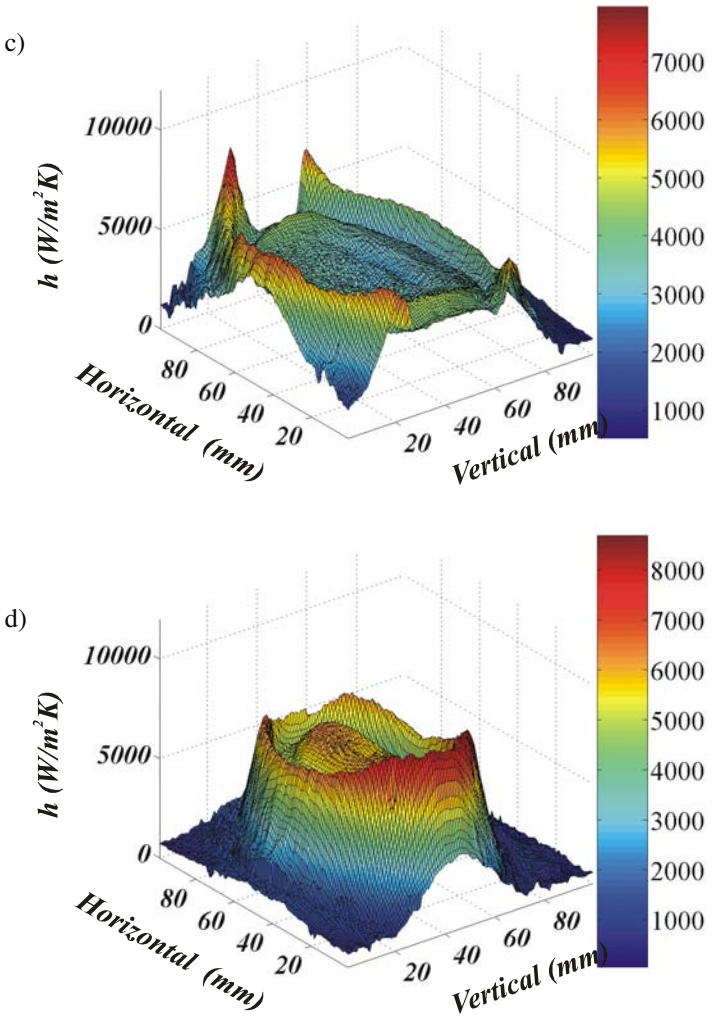

Figure .6. Surface plot of a) the film boiling heat transfer coefficient, b) initiation of CHF, c) the radial movement of the heat transfer coefficient from the centre outwards and d) a snap shot of the spatial heat transfer distribution showing a region at the centre of the wetted region where the heat transfer regime is due to single-phase solid-fluid interaction.

a)

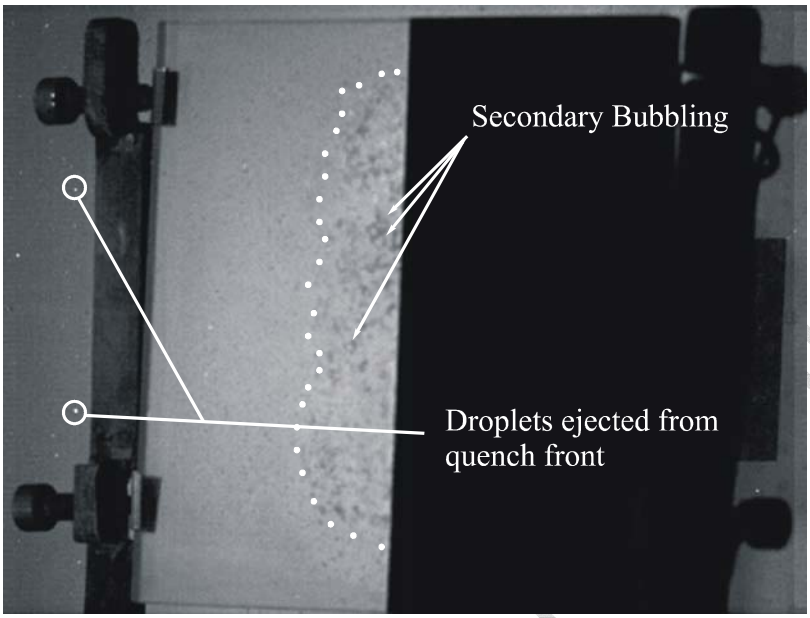

b)

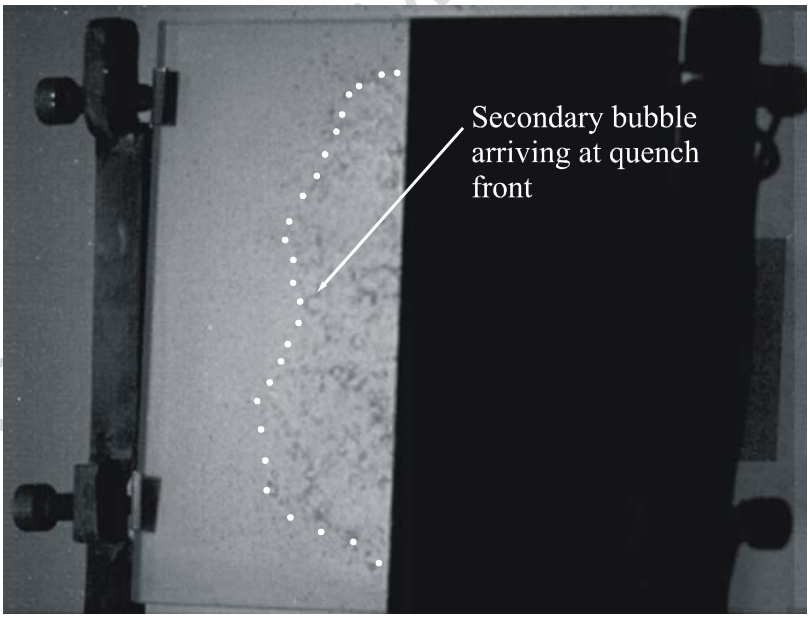

c)

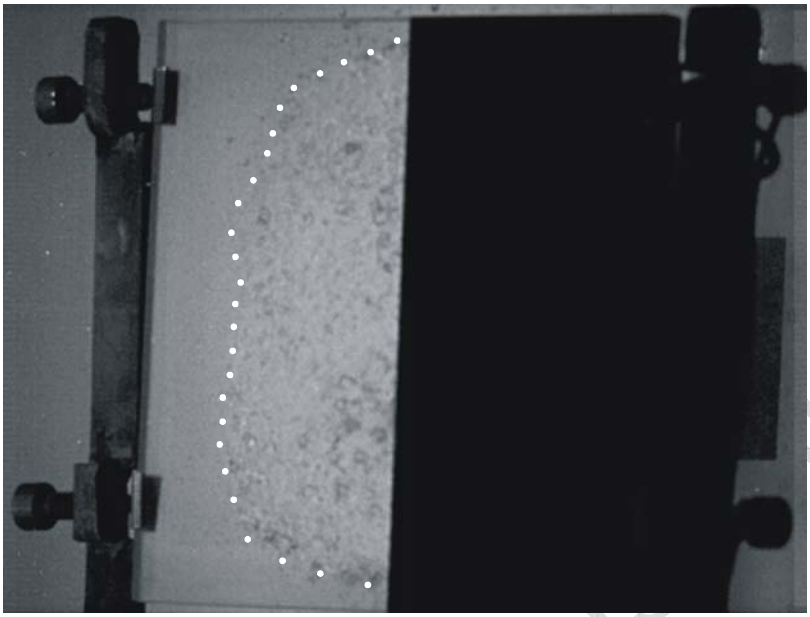

d)

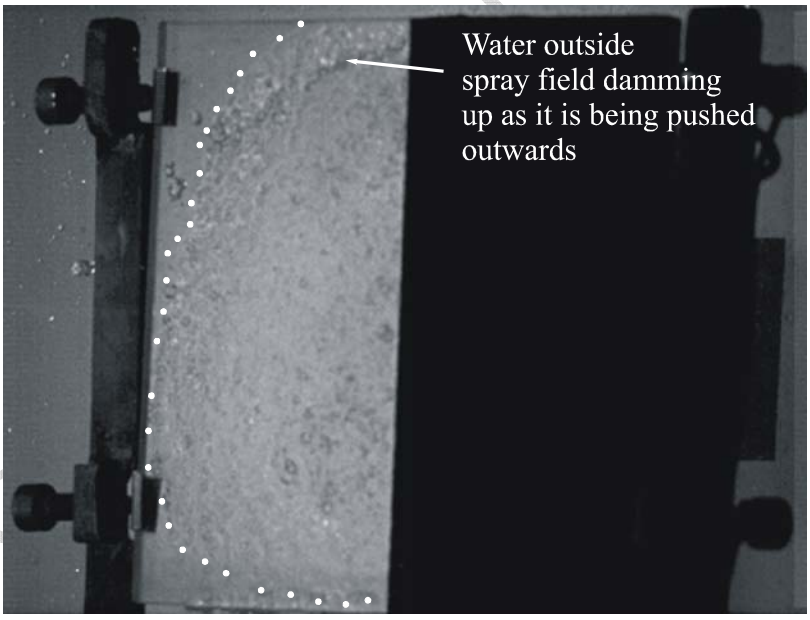

Figure .7. High speed images showing an unstructured movement of the quench front in time also indicating a) secondary bubbling and droplets leaving the heated surface, b) secondary bubble stagnation at quench front and c) accumulation of water as pool moves outside the spray field.

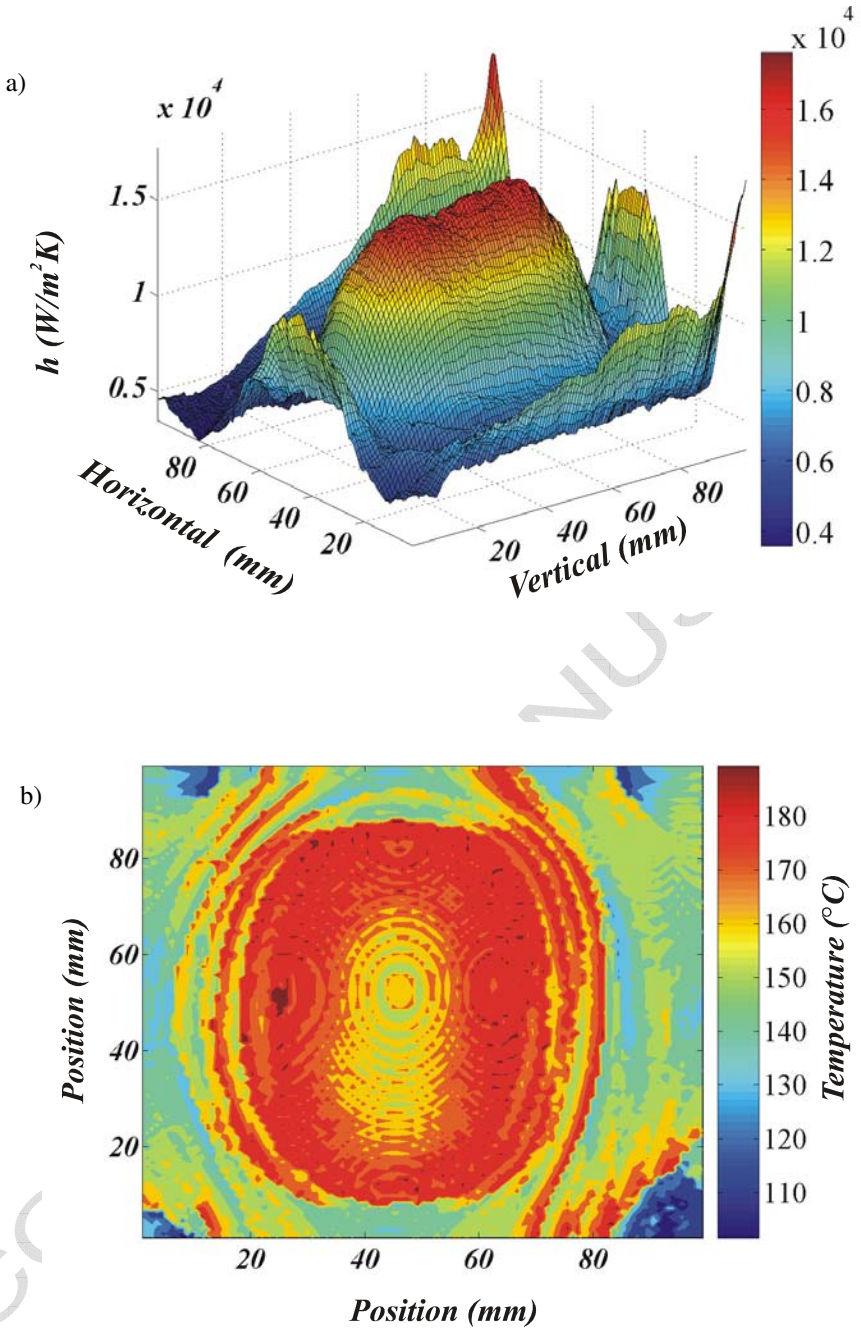

Figure .8. a) Surface plot of the spatial distribution of the CHF. b) Contour plot of T_{CHF}.

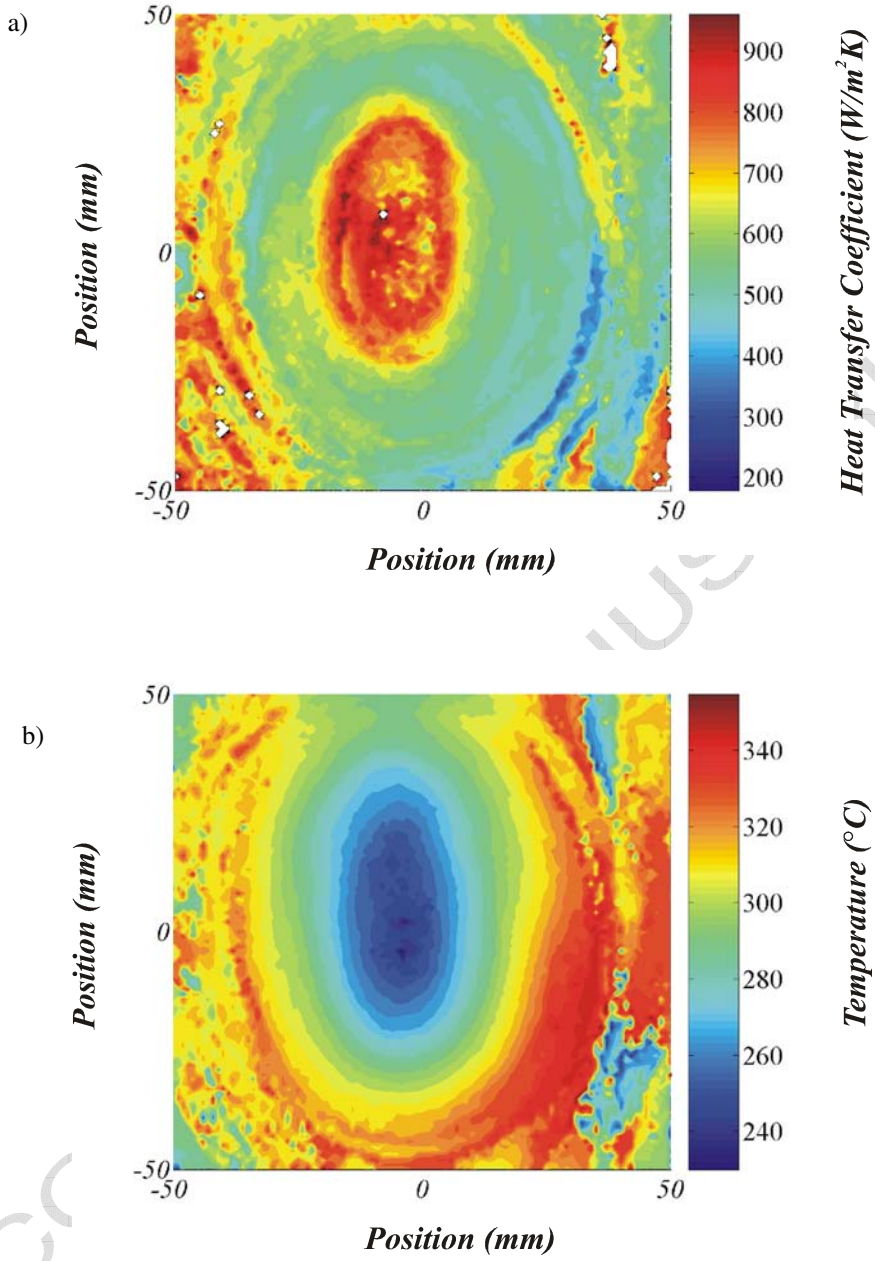

Figure .9. Contour plots of the a) minimum heat transfer coefficient and b) the Leidenfrost distribution.

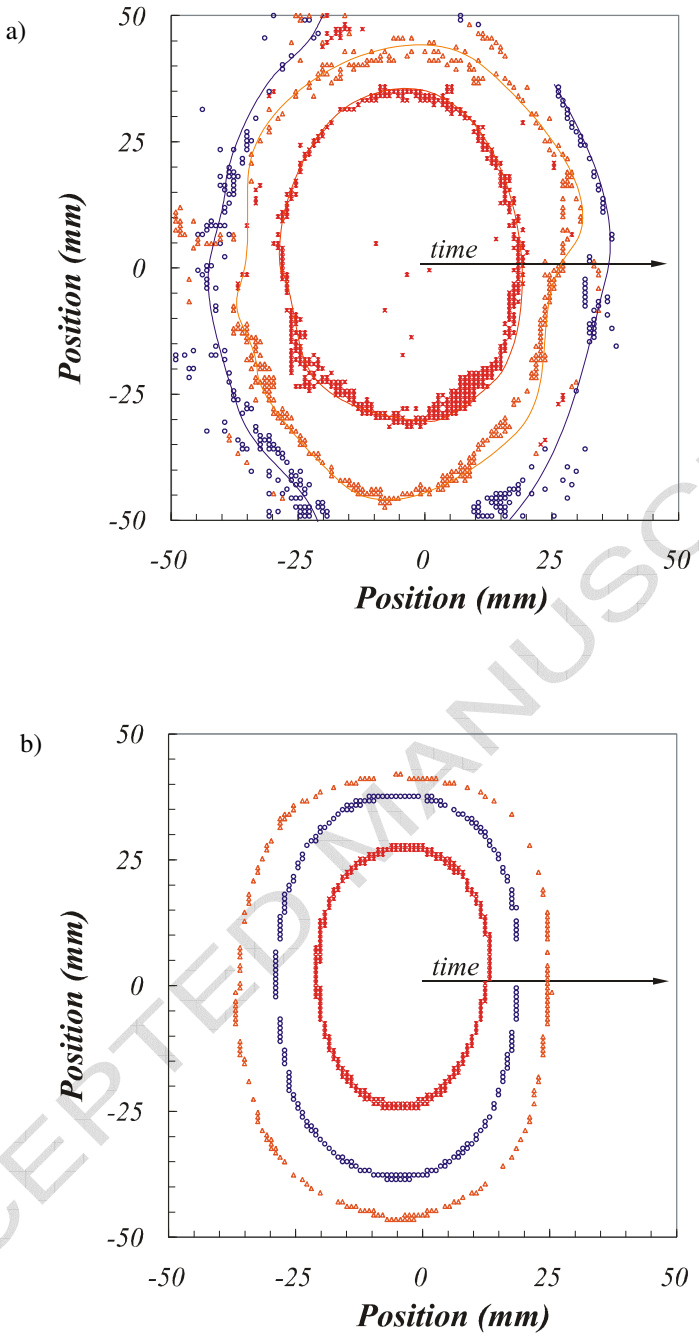

Figure .10. A representation of the position of the a) quench front and b) the CHF as a function of time moving radially outward.

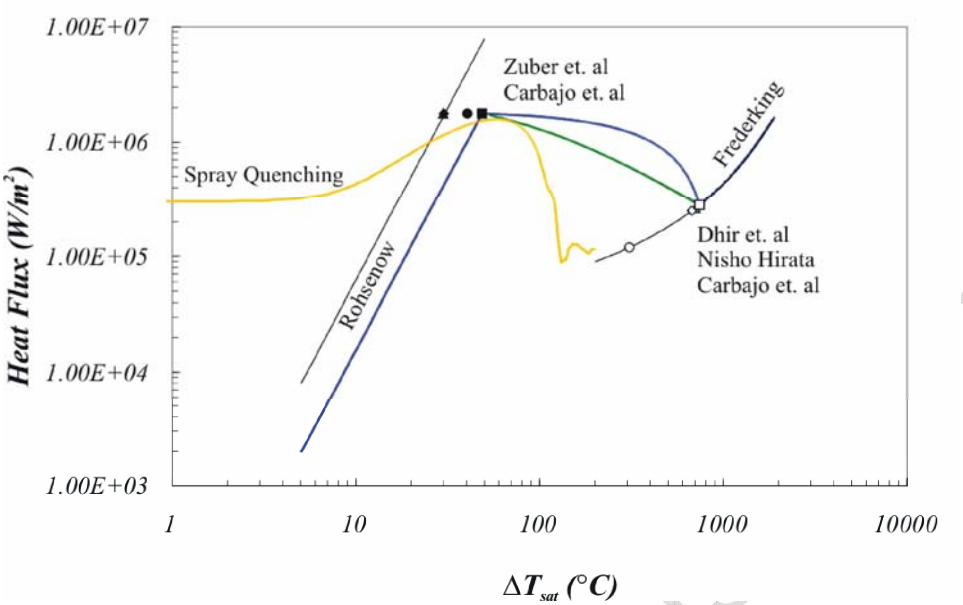

Figure .11. Comparison of boiling curve resulting from a spray with that experienced in a bath.

8. FIGURE CAPTIONS

Figure 1. Schematic of the experimental set up used in the heat transfer characterisation experiments.

Figure 2. Schematic showing the possible situations used to determine the search direction in the inverse heat transfer coefficient calculation.

Figure 3. Plot of a) the total flow rate as a function of operating pressure, b) droplet velocity and c) droplet size distribution along the long axis of the spray.

Figure 4. a) 2D Spray flux distribution of JAQ1153 and b) spray flux along the nozzles long and short axis.

Figure 5. a) Surface plot of a typical thermograph measured using Infrared thermography. b) Temporally fitted temperature response of a point on thermograph.

Figure 6. Surface plot of a) the film boiling heat transfer coefficient, b) initiation of CHF, c) the radial movement of the heat transfer coefficient from the centre outwards and d) a snap shot of the spatial heat transfer distribution showing a region at the centre of the wetted region where the heat transfer regime is due to single-phase solid-fluid interaction.

Figure 7. High speed images showing an unstructured movement of the quench front in time also indicating a) secondary bubbling and droplets leaving the heated surface, b) secondary bubble stagnation at quench front and c) accumulation of water as pool moves outside the spray field.

Figure 8. a) Surface plot of the spatial distribution of the CHF. b) Contour plot of T_{CHF}.

Figure 9. Contour plots of the a) minimum heat transfer coefficient and b) the Leidenfrost distribution.

Figure 10. A representation of the position of the a) quench front and b) the CHF as a function of time moving radially outward.

Figure 11. Comparison of boiling curve resulting from a spray with that experienced in a bath.

9. NUMENCLATURE

Q	[m^3/s]	Flow rate
q_i	[m^3/m^2s]	Flow Rate at Location
T	[°C]	Temperature
h	[W/m^2K]	Heat transfer Coefficient

Greek Symbols		
γ		Smoothing Parameter
λ		Fitting Parameter
τ	[s]	Time
ξ		Spray field limits
ζ		Spline knots

Subscripts	
CHF	Critical Heat Flux
MIN	Minimum heat flux condition